Applied Materials Today 7 (2017) 47–54

Contents lists available at ScienceDirect

Applied Materials Today

journal homepage: www.elsevier.com/locate/apmt

Oil tea shell derived porous carbon with an extremely large specific surface area and modification with MnO_2 for high-performance supercapacitor electrodes

Meng Zhou[a], Joshua Gomez[a], Binsong Li[b], Ying-Bing Jiang[c], Shuguang Deng[a,d,*]

[a] Department of Chemical & Materials Engineering, New Mexico State University, Las Cruces, 1040 S. Horseshoe Drive, NM 88003, United States
[b] Tsinghua Innovation Center in Dongguan, 4th Floor, Building 8, Sci & Tech. Innovation Park, Songshan Lake National High-Tech Industrial Development Zone, Dongguan City, Guangdong Province, PR China
[c] TEM/FIB Lab., University of New Mexico, Northrop Hall, Room B23, Albuquerque, NM 87185, United States
[d] School for Engineering of Matter, Transport and Energy, Arizona State University, 551 E. Tyler Mall, Tempe, AZ 85287, United States

ARTICLE INFO

Article history:
Received 6 October 2016
Received in revised form 23 January 2017
Accepted 24 January 2017

Keywords:
MnO_2
Activated carbon
Rate capability
Cycle stability
Energy density

ABSTRACT

Activated carbon (AC) with an extremely large specific surface area (2851 m^2/g) and large pore volume (2.68 cm^3/g) was derived from bio-waste oil tea shells by using $ZnCl_2$ as the activation agent. The porous carbon had a high amount of CO_2 adsorption (3.61 mmol/g) at ambient conditions (25 °C, 1 bar). Comprehensive characterizations including XRD, Raman, SEM, TEM, and TGA proved graphite existed in the AC samples. However, the capacitance (146 F/g @ 0.5 A/g) was in the normal range of carbon materials. By coating with a thin layer of MnO_2, the capacitance of MnO_2/AC was enhanced significantly (1126 F/g @ 0.5 A/g) without sacrificing the rate capability and cycle stability, even though the surface area was reduced to 23 m^2/g and pore volume reduced to 0.05 cm^3/g. A two-electrode (MnO_2/AC//AC) supercapacitor cell was set up, the energy density reached 24 Wh/kg with a power density of 275 W/kg.

1. Introduction

Recently, Tesla Motors announced that its new battery powered car (model 3) would be on the market by the end of 2017. The new car has several features including: 5 star safety, 0–60 mph within 6 s, a range of 215 miles per charge, and a battery that can be charged in minutes [1]. Clean energy is gaining popularity, and eventually may replace traditional fossil fuels in the car market. A battery delivers high energy density with low power density, which is good for long distance running, but poor for acceleration. Due to the limited tolerance of high current density, the charging time of a battery is normally very long (up to hours). In order to achieve the outstanding features mentioned by Tesla, these batteries must work alongside supercapacitors [2–5].

A supercapacitor has the following merits: high powder density, fast charge–discharge cycle, long cycle stability, low cost, and environmental benign. Based on the above properties, a supercapacitor can provide optimal power for high-speed acceleration and perform under high current density (~100 A/g) for quick charge [6]. Supercapacitors are also widely used in daily life, for instance: energy backup systems, emergency systems in airplanes and high speed trains [7,8]. Supercapacitors can be divided into two main categories: Electric Double Layer Capacitor (EDLC) and Pseudo Capacitor (PC). In EDLCs, the capacitance occurs under accumulations of charge at the electrode/electrolyte interfaces; the charge accumulations originate from the static force between the different charges. Unlike PC's capacitance, which depends on the revisable faradic reactions of the electrode and electrolyte [9]. Compared to PC, EDLC has a higher chemical and mechanical stability, lower electric resistance, and longer life span. The electrodes in EDLC are usually compiled of carbon materials, such as activated carbon (AC), carbon nanotube, graphene and fullerene [10–12]. Among these carbon materials, AC is the mostly used due to its high surface area, comparably high conductivity, chemical and physical stability, controllable pore sizes, low cost, simple synthesis, easy combination with other materials, and naturally occurring abundant sources. The gas absorbing property of AC is directly related to the surface area and pore volumes, the higher, the better. Although, for ion adsorption in the solutions, the process is very different, which causes the unexpected relationships among surface areas, pore volumes and capacitances. Zhao and Raymundo-Pinero et al. proved under certain conditions that the capacitance decreases even if the surface areas increases [13–15], this is due to small pore sizes and unsuitable pore shapes. Chmiola and Largeot et al. pointed out that the optimum pore sizes are 0.7 nm and 0.8 nm for the aqueous

* Corresponding author at: School for Engineering of Matter, Transport and Energy, Arizona State University, 551 E. Tyler Mall, Tempe, AZ, 85287, United States.
E-mail address: Shuguang.deng@asu.edu (S. Deng).

http://dx.doi.org/10.1016/j.apmt.2017.01.008
2352-9407/

electrolyte and organic electrolyte [16,17]. They suggest that pursuing a high surface area is not the proper way to get a high capacitance. The theoretical capacitance of EDLC is much lower than that of PC due to the transferred electrons per unit (mass, area, and volume). PC electrodes are normally made of metal oxides or metal nitrides [6–12,14,15,18–21]. MnO_2 is one of the most commonly used electrode materials, because of its multifarious valance states, high theoretical capacitance, low price, and non-toxic properties. In MnO_2 crystals, different internal mesoporous tunnels can be created with point, side, and surface sharing, which benefit the charge storage and ion transportations [22–24]. However, the conductivity of MnO_2 is low (10^{-5}–10^{-6} S/cm) [25] and the MnO_2 particles are easy to agglomerate together which reduces the active sites on the electrode surface, lowering the supercapacitor's rate capability, cycle stability and capacitance. To solve these problems, MnO_2 is often combined with AC's supporting matrix to enhance the electron transportation and disperse the particles uniformly.

The main purpose of this research was to combine the outstanding properties of AC and MnO_2 together to get the synergetic contributions from both the materials. The AC (used for this project) was derived from bio-waste oil tea shells from China, it had a very large surface area (>2800 m^2/g), a high pore volume (>2.5 cm^3/g), and high CO_2 adsorption uptakes (3.61 mmol/g at 1 bar, 25 °C). The capacitance was 146 F/g (@0.5 A/g, 1 M KOH solution), which is in the normal range of AC (20–300 F/g) [9], but smaller than most of the recently reported results [6,26–28]. Hereby, we took the advantage of large surface areas of AC to adsorb the MnO_2 particles directly on the surface forming a thin film-like coating. Although the BET surface area was reduced to 23 m^2/g, the active redox areas and the charge transfer were greatly enhanced, which improved the specific capacitance significantly (1126 F/g @ 0.5 A/g and 975 F/g @ 4 A/g).

2. Experimental

Preparation of AC: Bio-waste oil tea shells from China were ground in a coffee grinder (KRUPS F203) to get a fine powder. The powder was mixed together with $ZnCl_2$ (Sigma Aldrich, purity ≥98%) according to the impregnation ratio 1:3. The mixture was put into a 200 ml beaker and 150 ml DI water was added. The beaker was heated at 110 °C with stirring @ 400 rpm on a hot plate (Fisher Scientific) until a slurry was obtained. The slurry was then transferred to a boat crucible and put in a tube furnace (Lindberg blue M), heated at 550 °C for 1 h with N_2 gas flow (flow rate 300 sccm). The obtained sample was put in a 200 ml beaker with 100 ml 1 M HCl and heated at 70 °C and stirred @ 400 rpm for 1 h. The formed colloid was kept still for 20 h until most of the carbon particles deposited on the bottom of the beaker, then the solution was carefully removed. The above procedure was repeated multiple times by adding 150 ml DI water to wash the carbon particles until the pH value was close to 7. The obtained samples were dried in an oven (Fisher isotemp oven, 300 series) at 90 °C for 3 days.

Preparation of MnO_2/AC: 0.2 g of prepared AC was transferred to a beaker, adding 200 ml DI water, stirring @ 800 rpm until AC particles were uniformly dispersed in the water. 0.95 g $KMnO_4$ (Sigma Aldrich, purity ≥99.0%) was added to the solution and stirred for 18 h at room temperature. The solution was kept still overnight. After which the solution was filtered and washed 3 times with DI water, the obtained particles were dried in the oven for 24 h.

2.1. Characterization

The AC samples were measured by Raman spectrum (Renishaw inVia Microscope, λ = 633 nm). The crystal structure of the MnO_2/AC composite was determined by powder X-ray diffraction (XRD, Rigaku Miniflex II) with copper Kα radiation (λ ≈ 1.54 Å). The surface morphology and microstructure were characterized by High Resolution Transmission Electron Microscope (HRTEM JEOL-2010F with 200 kV accelerating voltages), Scanning Electron Microscope (SEM, FEI Quanta 3D FEG) with Energy-dispersive X-ray Spectroscopy (EDXS), and Atomic Force Microscope (AFM, Bruker Dimension Fastscan). The MnO_2 content was determined by a PerkinElmer Pyris 1 thermogravimetric analyzer (TGA) in the temperature range of 25–800 °C at a heating rate of 10 °C/min with oxygen (ultra high purity, Airgas) flow rate of 10 ml/min. The Brunauer-Emmet-Teller (BET) surface areas, pore volumes, and pore size distributions were measured by nitrogen adsorption and desorption isotherms at 77 K using a Micromeritics ASAP2050 Surface Area and Porosity Analyzer, the samples were de-gassed for 12 h at 110 °C before measurements.

2.2. Electrochemical test

90 mg of the obtained AC sample was combined with 10 mg polyvinylidene fluorides (PVDF) and 90 mg MnO_2/AC sample was combined with 10 mg PVDF by careful grinding. The two were mixed in 5 ml N-methyl-2-pyrrolidinone (NMP) solvent separately, stirring for 24 h. The obtained slurry (1.15 mg) was coated uniformly on a graphite substrate (1 cm × 1 cm) and dried in a vacuum oven at 80 °C for 12 h. Galvanostatic Charge/Discharge (GCD) tests (LAND CT2001A) and Cyclic Voltammetry (CV) tests (VersaSTAT 4) were performed at room temperature, by applying the standard three electrodes method (AC and MnO_2/AC as the working electrodes separately, Ag/AgCl as the reference electrode and platinum foil as the counter electrode) in 1 M KOH (99.98%, Alfa Aesar) electrolyte. Electrochemical Impedance Spectrum (EIS) was studied in the frequency range from 0.01 Hz to 100 kHz with amplitude of 5 mV at the open circuit potential (CHI-660).

3. Results and discussion

The phases of AC and MnO_2/AC were studied by X-ray diffraction as shown in Fig. 1a; the graphitic peaks at 26.54° and 45.4° suggested that graphitic phase existed in the AC (JCPDS No. 75-1621) [29,30]; the magnified XRD for AC was shown in Figure S1a. Most of the nano-particles inherited the structure of the biomass; there are certain amount of such sp^2 hybrid structures in oil tea shells, after carbonization, they converted to graphitic structure. This could be further proved by the Raman spectrum in Fig. 1b; the D band (sp^3) observed at 1350 cm^{-1} was related to the defects or disorders of the structure, the G band (sp^2) at 1580 cm^{-1} which could be related to the graphitic structure [31,32], $I_D/I_G \approx 1.27$. A weak peak of MnO_2 was also observed at 575 cm^{-1} (Figure S1b). The graphitic structure carbons might have originated from the bio-waste carbon source. After carbonization, the layer structures in the oil tea shell were inherited in the micro-structures of AC particles [33–36]. The microstructures were studied using the SEM and TEM, at low magnification (Fig. 1c), the carbon particles had flake shapes; at high magnification (Fig. 1d), the layered structures were clearly observed at the edge of the particles. The existence of graphite like layer structures not only increased the surface area, but also improved the conductivity of carbon materials, which benefited both adsorption and charge transportation [37,38]. After coating with MnO_2/AC, the layered structures were maintained (Figure S2). The XRD peaks of MnO_2/AC were indexed as the major phase of α-MnO_2 (JCPDS No. 42-1348) and minor phase of β-MnO_2 (JCPDS No. 24-735), weak graphitic peaks also existed (Fig. 1a). The doped MnO_2 particles were observed by TEM, and compared with the AC samples, the low magnification TEM (Fig. 2a) showed much rougher surface areas, at high magnification (Fig. 2b), the

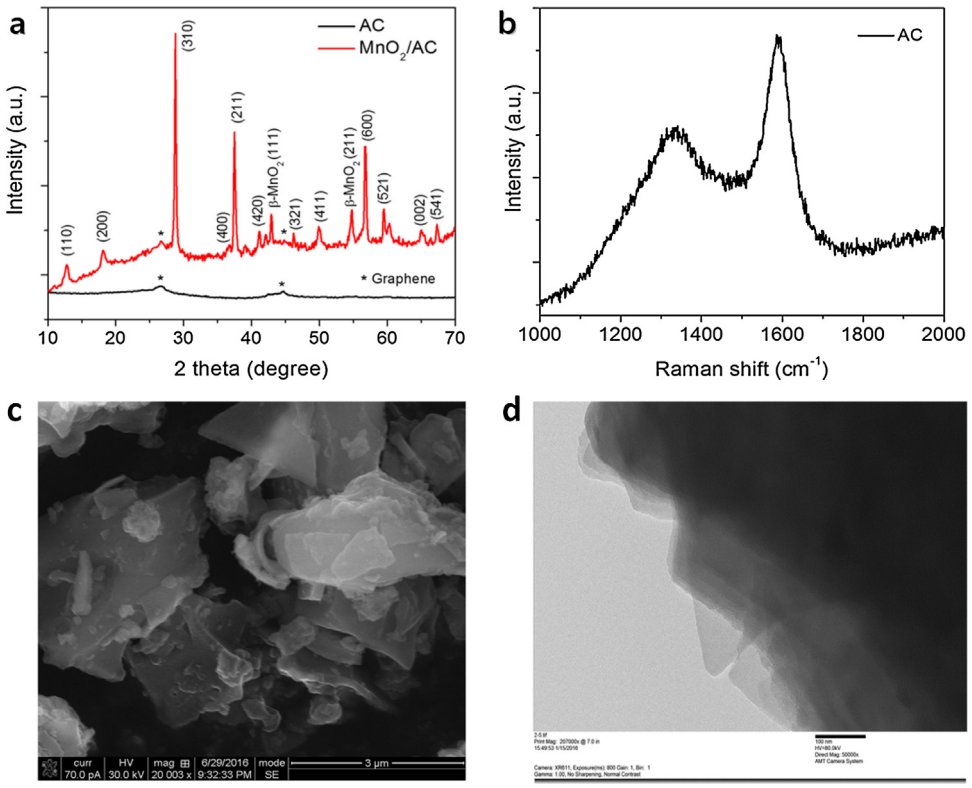

Fig. 1. (a) XRD of AC and MnO_2/AC; (b) Raman spectrum of AC; (c) SEM and (d) TEM of AC.

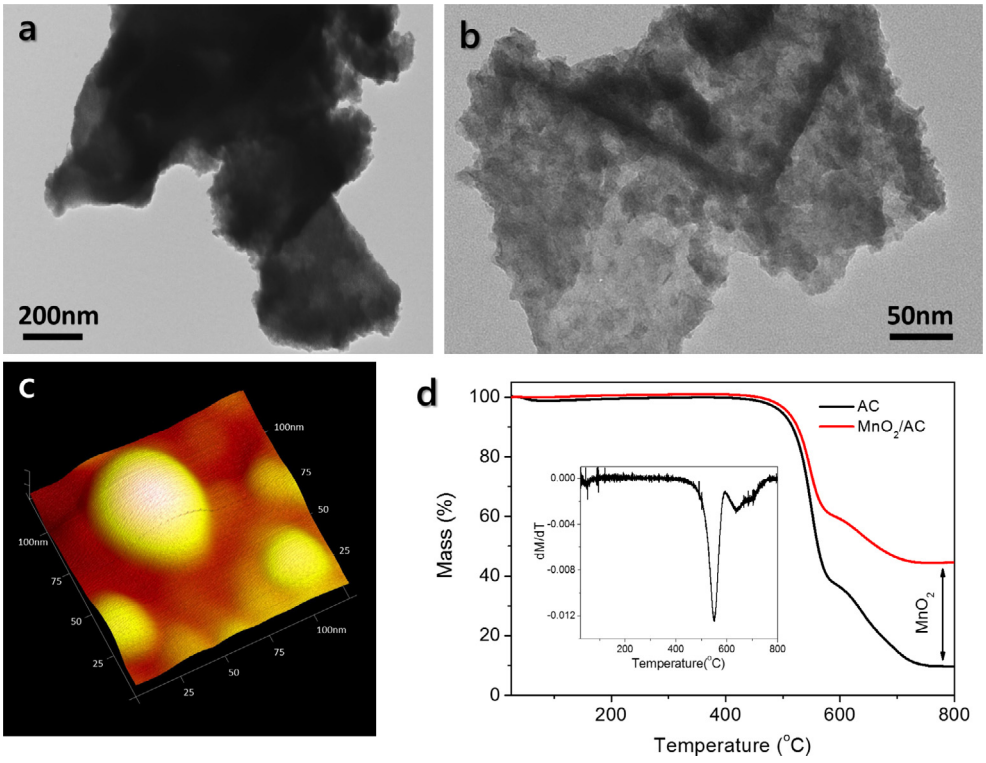

Fig. 2. (a) Low and (b) high magnification TEM of MnO_2/AC; (c) 3D AFM plot of MnO_2/AC; (d) TGA of AC and MnO_2/AC (inset: dM/dT vs. T).

AC surfaces covered with MnO_2 particles were clearly observed. The surface morphologies were also studied by AFM, the 3D plot of AFM (Fig. 2c) showed that the MnO_2 particles formed different size islands on the surfaces. The islands were connected by the AC matrix to form the complete conducting network. The MnO_2 particles were well dispersed and the thicknesses of the particle islands were below 100 nm, which was similar to a thin film partially coated on the carbon substrate. This created more redox active

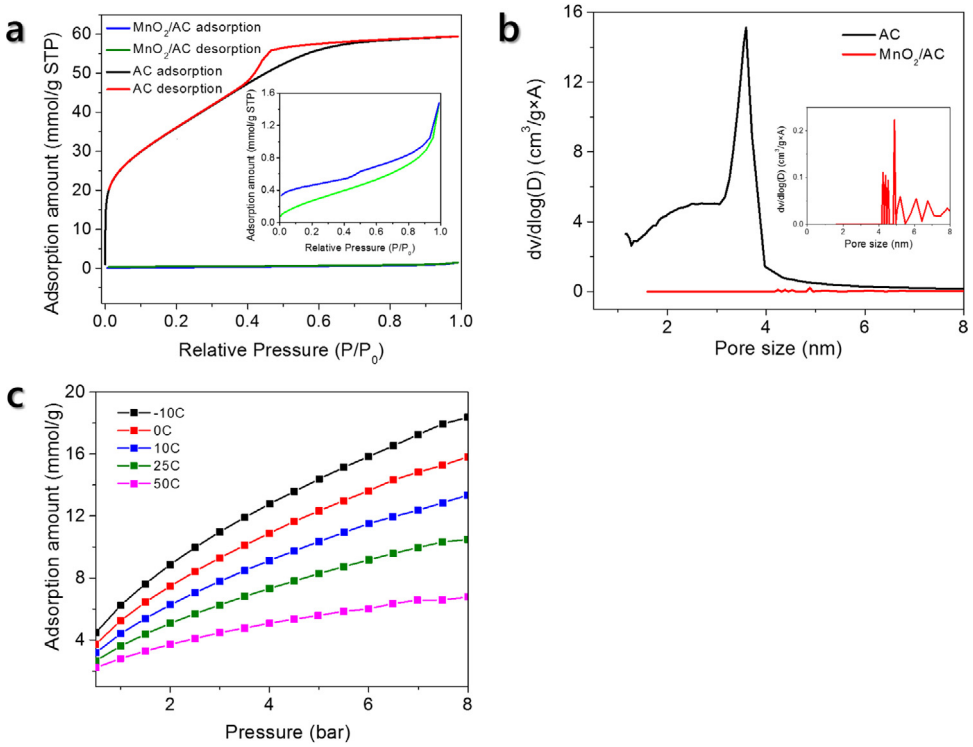

Fig. 3. (a) N_2 adsorption and desorption at 77 K of AC and MnO_2/AC (inset: MnO_2/AC); (b) pore size distribution of AC and MnO_2/AC (inset: MnO_2/AC); (c) CO_2 adsorption of AC.

sites and reduced the diffusion distance. The carbon matrix with the porous structure could also work as a buffer layer to release the strains which were caused by intercalation and de-intercalation of ions in the electrolyte during the charge and discharge process, preventing the structural failures. The distributions of Mn, O and C elements were further confirmed by STEM-EDS (Figure S3a–d), the three elements were uniformly mixed together, the signals of C were weak (Figure S3d), which might be due to the top coverage of Mn and O. The MnO_2 mass loading was measured by TGA (Fig. 2d). The AC sample residual was 9.7% (the residual might be the silicon and other inorganic compounds in the shells), for the MnO_2/AC sample, the residual was 44.5%, the calculated total mass loading of MnO_2 was 38.5%. The mass loading was also measured by EDS, Mn content was 23.4% (wt.%), same as 37% of MnO_2 (Figure S3e), this large loading helped to increase the specific capacitance. The first differentiation of mass to temperature (dM/dT) showed two main peaks at 550 °C and 630 °C (inset of Fig. 2d), which corresponded to amorphous carbon and graphite. This was another evidence of graphite existing in the samples. The BET surface areas, pore volumes and pore size distributions were measured by N_2 adsorption and desorption isothermals at 77 K for both AC and MnO_2/AC samples as shown in Fig. 3a and b. The BET surface area of AC was 2851 m^2/g, the pore volume was 2.68 cm^3/g, the main region of pore size distributions was between 1 and 4 nm, and the average pore size is 2.70 nm. The large surface area and pore volume of AC could further be proved by CO_2 adsorption (Fig. 3c), at 0 °C and 1 bar (STP). The CO_2 adsorption amount was 5.24 mmol/g, at 25 °C and 1 bar (ambient condition), the CO_2 adsorption amount was 3.61 mmol/g, which was higher than most of the carbon materials reported by Yu et al. in his CO_2 adsorption review paper [39]. After coating with MnO_2 (insets of Fig. 3a and b), the surface area was reduced to 23 m^2/g with pore volume 0.05 cm^3/g, the pore sizes distribution was above 4 nm, and the average pore size was increased to 5.5 nm. Most of the pores were covered by MnO_2 particles. The pores (especially for the micropores) had large well-potential which easily attracted MnO_2 molecules in the solution, formed the nuclei centers and further developed into the MnO_2 islands on the surface. The adhesion between MnO_2 particles and the AC surface was very strong, preventing a loss of mass during the charging and discharge process. The surface of MnO_2/AC was further studied by HRTEM (Figure S4), a few uncovered pores with diameters 2–8 nm could be observed (circled in red).

The cyclic voltammetry (CV) tests of AC and MnO_2/AC electrodes were shown in Fig. 4a and b separately. The AC sample curves showed quasi-rectangle shapes at low scan rates (5 mV/s, 10 mV/s), which was typical EDLC behavior. At a high scan rate (50 mV/s and 100 mV/s), the rectangular shapes were highly distorted, this distortion was caused by the internal electronic resistances and irreversible ion diffusions in the micropores. The MnO_2/AC sample curves showed very strong oxidation and reduction peaks, the suggested revisable redox reactions as the following [32,40,41]:

$$MnO_2 + nK^+ + ne^- \leftrightarrow MnOOK_n$$

According to the formula:

$$c = \frac{n \times F}{M \times V} \quad (1)$$

where c is the specific capacitance, n is the number of electrons transferred in one molar electrode material during the redox reaction, F is the Faradic constant, M is the molar weight of the electrode materials and V is the voltage window [42].

The capacitance depended on how many K^+ ions (n) could be intercalated and de-intercalated during the charge and discharge process. The number of active redox sites played an important role, by adsorption of the MnO_2 particles on the large surface area of AC. The active sites were greatly enhanced and the ion diffusion distances were reduced, resulting in the achievement of high capacitance. It was observed that the oxidation peaks shifted to a higher potential and reduction peaks shifted to a lower potential with the increasing of scan rates, which proved that the ion diffusions at

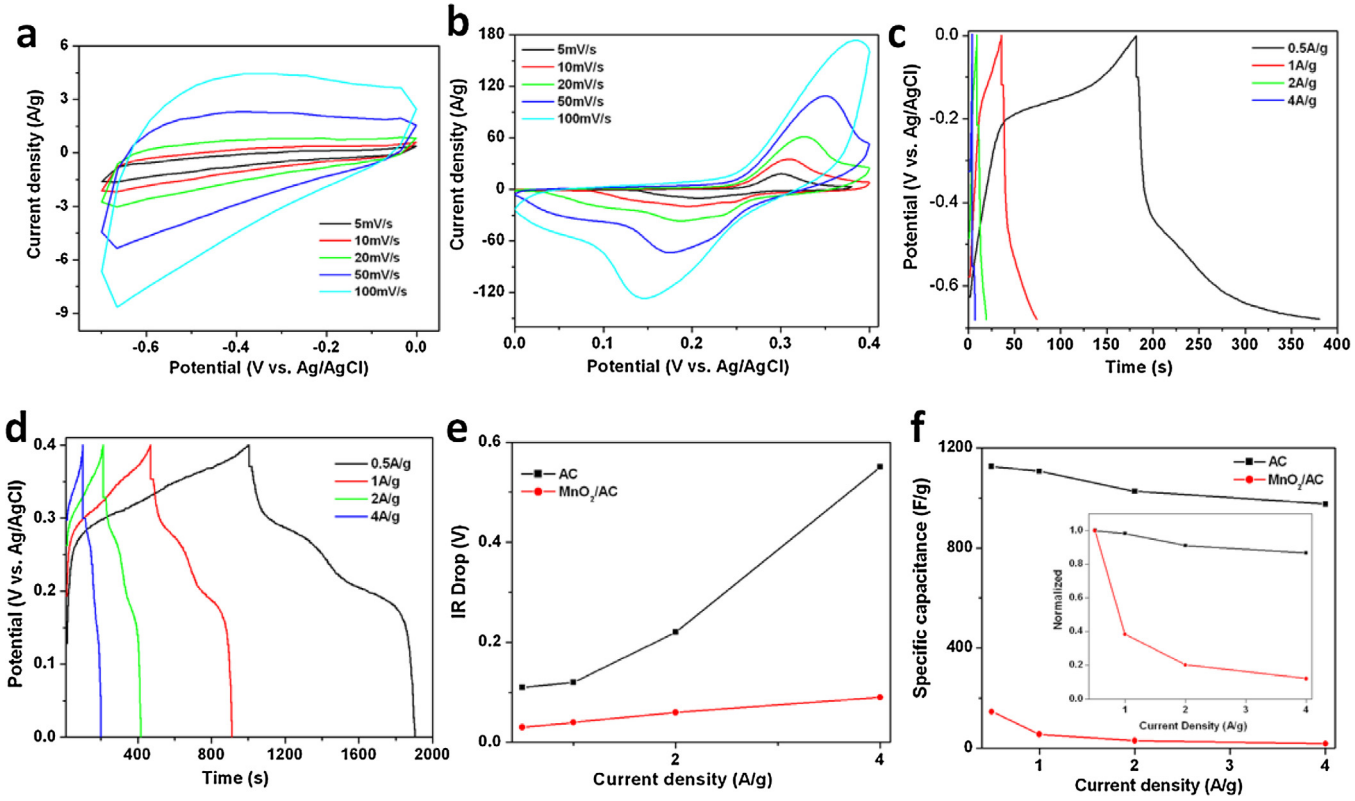

Fig. 4. (a and b) CV of AC and MnO_2/AC; (c and d) GCD of AC and MnO_2/AC; (e) IR drops and (f) rate capability (inset: normalized) of AC and MnO_2/AC.

high scan rates required more energy. This phenomenon also had a connection with the electrode polarization [43,44].

The Galvanostatic Charge/Discharge (GCD) tests were shown in Fig. 4c and d, both curves are asymmetric. The nonlinear parts of AC were caused by the near saturation of the ions on the surfaces [41]. Two humps appeared in the discharge curves of MnO_2/AC, corresponding to two redox reactions, these were due to the multifarious valence states of MnO_2. With increasing the scan rates, the corresponding IR drops increased for both samples, which were: 0.11 V, 0.12 V, 0.22 V, and 0.55 V for AC and 0.03 V, 0.04 V, 0.06 V, and 0.09 V for MnO_2/AC at the scan rate of 0.5 A/g, 1 A/g, 2 A/g, and 4 A/g correspondingly. The comparison of IR drops was shown in Fig. 4e. The mechanism of EDLC is the charge accumulations at the interfaces between electrode and electrolyte caused by the electrostatic force of different charges. For AC, the capacitance is mainly from the charge storage in micropores. Before entering the micropore, the solvated ions in the electrolyte had to go through desolvation or distortion to fit the micropore size [14–17,41,45,46], which produced large resistances when ions diffused in and out of the micropores, reflected by the high IR drops. For the MnO_2/AC electrode, a majority of the pores were covered on the surface by MnO_2 particle islands. The thickness of the islands was less than 100 nm measured by AFM, which reduced the ion diffusion distances and resistances, proved by the low IR drops.

The specific capacitance was calculated from GCD, according to the formula:

$$C = \frac{I \times \Delta t}{m \times V} \tag{2}$$

where Δt is the discharge time and m is the mass of electrode materials.

The calculated specific capacitances in correlation to current densities (rate capability) were shown in Fig. 4f, the inset was the normalized rate capability. It was obvious that by applying this simple coating method, not only the specific capacitance was enhanced significantly, but also the rate capability was improved greatly. The micropores did not play an essential role in the supercapacitor, avoiding the high diffusion resistances. The obtained specific capacitances of MnO_2/AC were 1126 F/g @ 0.5 A/g and 975 F/g @ 4 A/g. The specific capacitance of the MnO_2/AC composition is much higher than that of the pristine activated carbon (146 F/g @ 0.5 A/g), and it is still slightly lower than a recent literature value (1405 F/g) on a polyaniline/mesoporous manganese dioxide composite [47].

The cycle stability (tested at 1 A/g) shown in Fig. 5a and its inset (normalized cycle stability), after 3000 cycles, AC and MnO_2/AC remained 86% and 97% of the initial capacitances separately. Due to the low ion diffusion resistances, MnO_2/AC showed a better cycle stability than AC. The impedance measurements of AC and MnO_2/AC were shown in Fig. 5b, the equivalent series resistance (ESR) of MnO_2/AC was 0.73 Ω (inset, high frequency), almost the same as that of AC. However, the diameter of the hemi circle for MnO_2/AC was 0.71 Ω (high to middle frequency), much smaller than that of AC, which represented lower ion diffusion resistance.

In order to test the practical use of obtained AC and MnO_2/AC, a two-electrode supercapacitor cell was built using the MnO_2/AC as the positive electrode (+) and AC as the negative electrode (−). The mass calculation was based on:

$$Q_+ = Q_- \quad m_+c_+V_+ = m_-c_-V_- \tag{3}$$

where Q is the charge.

Using 1.2 mg MnO_2/AC as positive electrode, the corresponding mass of AC for the negative electrode was calculated to be 5.3 mg, the total mass for the whole supercapacitor cell is 6.5 mg. CV curves (Fig. 5c) show distortions from rectangular shapes at high scan rates (50 mV/s, 100 mV/s) due to the irreversible diffusion resistances in the micropores of the AC. The GCD measurements were shown in Fig. 5d, the corresponding specific capacitances (c) were calculated

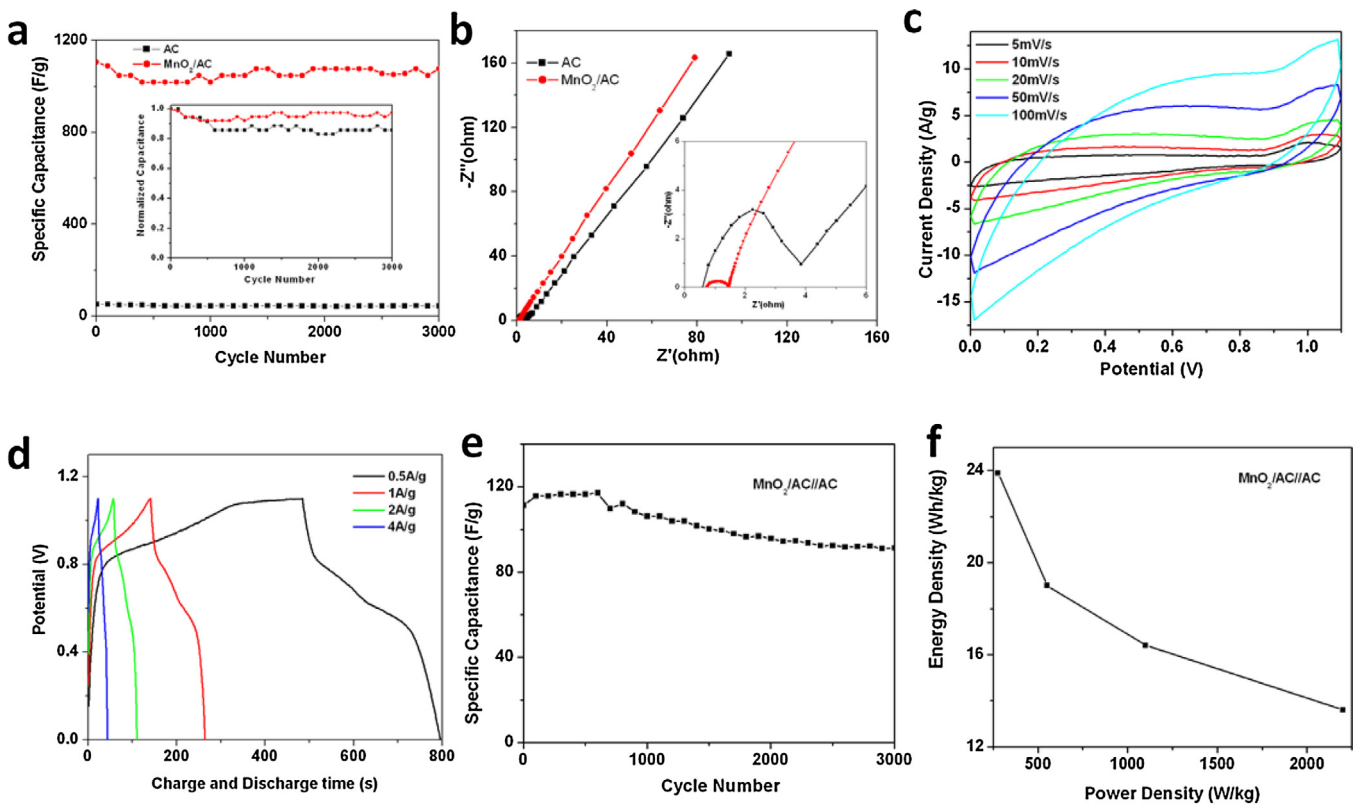

Fig. 5. (a) Cycle stability @ 1 A/g of AC and MnO_2/AC (inset: normalized cycle stability); (b) EIS measurement of AC and MnO_2/AC (inset: high frequency region); (c) CV of MnO_2/AC//AC; (d) GCD of MnO_2/AC//AC; (e) cycle stability @ 1 A/g of MnO_2/AC//AC; (f) energy density vs. power density of MnO_2/AC//AC.

(141 F/g @ 0.5 A/g, 81 F/g @ 4 A/g). The cycle stability of the whole supercapacitor cell was measured at 1 A/g (Fig. 5e), a retention of 81% of initial capacitance remained after 3000 cycles.

The energy density and power density were calculated according to the formulas [48]:

$$E\ (\mathrm{Wh/kg}) = \frac{1}{2}cV^2 \times \frac{1}{3.6} \quad (4)$$

$$P(\mathrm{W/kg}) = \frac{E}{t} \quad (5)$$

where E is the energy density, P is the power density, and t is the discharge time.

The energy density vs. power density was shown in Fig. 5f. The asymmetric supercapacitor possessed the energy density 23.9 Wh/kg @ power density 275.4 W/kg and 13.6 Wh/kg @ 2.2 kW/kg, compared with the published works which had AC as the negative electrode, it was higher than device $Ni(OH)_2$/GNs/NF//AC (11.1 Wh/kg @ 93 W/kg) [49], device $NiCo_2O_4$ NSs @ HMRAs//AC ASC (15.4 Wh/kg @ 700 W/kg) [50], device MnO_2 @ Carbon black//AC (11 Wh/kg @ 50 W/kg) [51]. Even though it was almost identical to device Ni_xCo_{1-x}LDHs//AC (23.7 Wh/kg @ 284.2 W/kg) [52], device $NiCo_2O_4$-rGO//AC (23.32 Wh/kg @ 324.9 W/kg) [53], the procedure to make the electrodes was much simpler and easier and the cost of precursors and raw materials (bio-wastes) were much cheaper, which makes it possible to scale up the production from laboratory level to industry level.

4. Conclusions

Activated carbons were derived from bio-waste oil tea shells by using $ZnCl_2$ as the activation agent. The porous carbon had a layered microstructure with an extremely large specific surface area (2851 m^2/g) and pore volume (2.68 cm^3/g). XRD, Raman spectra, SEM and TEM further proved that there was a certain amount of graphite present, which improved the bulk conductivity and expanded the surface area. The CO_2 adsorption amount (3.61 mmol/g) at ambient conditions (25 °C, 1 bar) were consistent with the high surface and pore volume. Although, the capacitance (146 F/g @ 0.5 A/g) was just in the normal range of carbon materials, it mainly came from the charge storage of the micropores, which inherited a high resistance to ion diffusions. By coating a thin layer of MnO_2 (<100 nm), the capacitance was enhanced significantly (1126 F/g @ 0.5 A/g). The large surface area of AC helped to disperse the MnO_2 particles into thin-film-like islands on the surface. This increased the mass loading of MnO_2 and created large redox active sites, which resulted in the raising of the charges transferred during the reactions (n). The internal tunnels of MnO_2 benefited the ion transportation and storage. The AC matrix worked as the fast lanes for charge transportation to reduce the electric resistances and get a good rate capability. The highly porous structure of AC not only increased the adhesion between particles and surface, but also worked as a buffer layer to release the strains caused by the ion intercalation and de-intercalation during the charge discharge process. The buffer layer prevented the mechanical breakdown and increased the cycle stability. After 3000 cycles (tested @1 A/g), there was about 97% remaining of the initial capacitance which was better than that of the pure AC (86%). Further calculations showed that the energy density could reach 23.9 Wh/kg @ power density of 275 W/kg, which has the potential for practical uses.

Acknowledgements

This project was partially supported by U.S. Department of Energy (DE-EE0006316) and US National Science Foundation (EEC-1028968, MRI-1229558, and #IIA-1301346). S. Deng

acknowledges the support from the Fulton Schools of Engineering at Arizona State University. The authors thank Miss Stephanie Richins for the language support.

Appendix A. Supplementary data

Supplementary data associated with this article can be found, in the online version, at doi:10.1016/j.apmt.2017.01.008.

References

[1] http://www.scpr.org/programs/take-two/2016/04/01/47703/the-wheel-thing-tesla-model-3-drums-up-excitement/ and https://www.teslamotors.com/supercharger.
[2] A. Du Pasquier, I. Plitz, S. Menocal, G. Amatucci, A comparative study of Li-ion battery, supercapacitor and nonaqueous asymmetric hybrid devices for automotive applications, J. Power Sources 115 (1) (2003) 171–178.
[3] P. Simon, Y. Gogotsi, B. Dunn, Where do batteries end and supercapacitors begin? Science 343 (6176) (2014) 1210–1211.
[4] D.P. Dubal, O. Ayyad, V. Ruiz, P. Gomez-Romero, Hybrid energy storage: the merging of battery and supercapacitor chemistries, Chem. Soc. Rev. 44 (7) (2015) 1777–1790.
[5] G.P. Wang, L. Zhang, J.J. Zhang, A review of electrode materials for electrochemical supercapacitors, Chem. Soc. Rev. 41 (2) (2012) 797–828.
[6] H. Wang, Z.W. Xu, A. Kohandehghan, Z. Li, K. Cui, X.H. Tan, T.J. Stephenson, C.K. King'ondu, C.M.B. Holt, B.C. Olsen, J.K. Tak, D. Harfield, A.O. Anyia, D. Mitlin, Interconnected carbon nanosheets derived from hemp for ultrafast supercapacitors with high energy, ACS Nano 7 (6) (2013) 5131–5141.
[7] A. Ramadoss, S.J. Kim, Improved activity of a graphene–TiO_2 hybrid electrode in an electrochemical supercapacitor, Carbon 63 (0) (2013) 434–445.
[8] H.E.Z. Abidin, A.A. Hamzah, B.Y. Majlis, J. Yunas, N.A. Hamid, U. Abidin, Electrical characteristics of double stacked Ppy-PVA supercapacitor for powering biomedical MEMS devices, Microelectron. Eng. 111 (2013) 374–378.
[9] L.L. Zhang, X.S. Zhao, Carbon-based materials as supercapacitor electrodes, Chem. Soc. Rev. 38 (9) (2009) 2520–2531.
[10] Z. Hu, M.P. Srinivasan, Mesoporous high-surface-area activated carbon, Microporous Mesoporous Mater. 43 (3) (2001) 267–275.
[11] D.W. Wang, F. Li, M. Liu, G.Q. Lu, H.M. Cheng, 3D aperiodic hierarchical porous graphitic carbon material for high-rate electrochemical capacitive energy storage, Angew. Chem. Int. Ed. 47 (2) (2008) 373–376.
[12] G. Wang, H. Wang, X. Lu, Y. Ling, M. Yu, T. Zhai, Y. Tong, Y. Li, Solid-state supercapacitor based on activated carbon cloths exhibits excellent rate capability, Adv. Mater. 26 (17) (2014) 2676–2682.
[13] Z. Zhang, S.C. Mu, B.W. Zhang, L. Tao, S.F. Huang, Y.Z. Huang, F.M. Gao, Y.F. Zhao, A novel synthesis of carbon nanotubes directly from an indecomposable solid carbon source for electrochemical applications, J. Mater. Chem. A 4 (6) (2016) 2137–2146.
[14] Y.F. Zhao, W. Ran, J. He, Y.F. Song, C.M. Zhang, D.B. Xiong, F.M. Gao, J.S. Wu, Y.Y. Xia, Oxygen-rich hierarchical porous carbon derived from artemia cyst shells with superior electrochemical performance, ACS Appl. Mater. Interfaces 7 (2) (2015) 1132–1139.
[15] E. Raymundo-Pinero, K. Kierzek, J. Machnikowski, F. Beguin, Relationship between the nanoporous texture of activated carbons and their capacitance properties in different electrolytes, Carbon 44 (12) (2006) 2498–2507.
[16] J. Chmiola, G. Yushin, Y. Gogotsi, C. Portet, P. Simon, P.L. Taberna, Anomalous increase in carbon capacitance at pore sizes less than 1 nanometer, Science 313 (5794) (2006) 1760–1763.
[17] C. Largeot, C. Portet, J. Chmiola, P.L. Taberna, Y. Gogotsi, P. Simon, Relation between the ion size and pore size for an electric double-layer capacitor, J. Am. Chem. Soc. 130 (9) (2008) 2730–2731.
[18] H. Zhang, Y. Wang, P. Liu, S.L. Chou, J.Z. Wang, H. Liu, G. Wang, H. Zhao, Highly ordered single crystalline nanowire array assembled three-dimensional $Nb_3O7(OH)$ and Nb_2O_5 superstructures for energy storage and conversion applications, ACS Nano 10 (1) (2015) 507–514.
[19] C. Zhou, Y.W. Zhang, Y.Y. Li, J.P. Liu, Construction of high-capacitance 3D CoO@ polypyrrole nanowire array electrode for aqueous asymmetric supercapacitor, Nano Lett. 13 (5) (2013) 2078–2085.
[20] G. Hasegawa, A. Kitada, S. Kawasaki, K. Kanamori, K. Nakanishi, Y. Kobayashi, H. Kageyama, T. Abe, Impact of electrolyte on pseudocapacitance and stability of porous titanium nitride (TiN) monolithic electrode, J. Electrochem. Soc. 162 (1) (2015) A77–A85.
[21] C. Zhu, P. Yang, D. Chao, X. Wang, X. Zhang, S. Chen, B.K. Tay, H. Huang, H. Zhang, W. Mai, H.J. Fan, All metal nitrides solid-state asymmetric supercapacitors, Adv. Mater. 27 (31) (2015) 4566–4571.
[22] O. Ghodbane, J.-L. Pascal, F. Favier, Microstructural effects on charge-storage properties in MnO_2-based electrochemical supercapacitors, ACS Appl. Mater. Interfaces 1 (5) (2009) 1130–1139.
[23] R. Peng, N. Wu, Y. Zheng, Y. Huang, Y. Luo, P. Yu, L. Zhuang, Large-scale synthesis of metal-ion-doped manganese dioxide for enhanced electrochemical performance, ACS Appl. Mater. Interfaces 8 (13) (2016) 8474–8480.
[24] X.K. Huang, D.P. Lv, H.J. Yue, A. Attia, Y. Yang, Controllable synthesis of alpha- and beta-MnO(2): cationic effect on hydrothermal crystallization, Nanotechnology 19 (22) (2008).
[25] J. Zhi, O. Reiser, F. Huang, Hierarchical MnO_2 spheres decorated by carbon-coated cobalt nanobeads: low-cost and high-performance electrode materials for supercapacitors, ACS Appl. Mater. Interfaces 8 (13) (2016) 8452–8459.
[26] X. Wei, S. Wan, X. Jiang, Z. Wang, S. Gao, Peanut-shell-like porous carbon from nitrogen-containing poly-N-phenylethanolamine for high-performance supercapacitor, ACS Appl. Mater. Interfaces 7 (40) (2015) 22238–22245.
[27] Y.S. Yun, M.H. Park, S.J. Hong, M.E. Lee, Y.W. Park, H.-J. Jin, Hierarchically porous carbon nanosheets from waste coffee grounds for supercapacitors, ACS Appl. Mater. Interfaces 7 (6) (2015) 3684–3690.
[28] W. Xing, S.Z. Qiao, R.G. Ding, F. Li, G.Q. Lu, Z.F. Yan, H.M. Cheng, Superior electric double layer capacitors using ordered mesoporous carbons, Carbon 44 (2) (2006) 216–224.
[29] P.L. Walker, J.F. Rakszawski, A.F. Amington, Determination of graphitic and amorphous carbon, ASTM Bull. 208 (1955) 52–54.
[30] B.S. Girgis, Y.M. Temerk, M.M. Gadelrab, I.D. Abdullah, X-ray diffraction patterns of activated carbons prepared under various conditions, Carbon Sci. 8 (2) (2007) 95–100.
[31] D.S. Geng, Y. Chen, Y.G. Chen, Y.L. Li, R.Y. Li, X.L. Sun, S.Y. Ye, S. Knights, High oxygen-reduction activity and durability of nitrogen-doped graphene, Energ. Environ. Sci. 4 (3) (2011) 760–764.
[32] Z.P. Bai, H.J. Li, M.J. Li, C.P. Li, X.F. Wang, C.Q. Qu, B.H. Yang, Flexible carbon nanotubes-MnO_2/reduced graphene oxide-polyvinylidene fluoride films for supercapacitor electrodes, Int. J. Hydrogen Energy 40 (46) (2015) 16306–16315.
[33] J. Ding, H. Wang, Z. Li, K. Cui, D. Karpuzov, X. Tan, A. Kohandehghan, D. Mitlin, Peanut shell hybrid sodium ion capacitor with extreme energy-power rivals lithium ion capacitors, Energ. Environ. Sci. 8 (3) (2015) 941–955.
[34] S.T. Senthilkumar, R.K. Selvan, J.S. Melo, C. Sanjeeviraja, High performance solid-state electric double layer capacitor from redox mediated gel polymer electrolyte and renewable tamarind fruit shell derived porous carbon, ACS Appl. Mater. Interfaces 5 (21) (2013) 10541–10550.
[35] D. Kang, Q. Liu, J. Gu, Y. Su, W. Zhang, D. Zhang, "Egg-Box"-assisted fabrication of porous carbon with small mesopores for high-rate electric double layer capacitors, ACS Nano 9 (11) (2015) 11225–11233.
[36] Y. Ren, Q. Xu, J. Zhang, H. Yang, B. Wang, D. Yang, J. Hu, Z. Liu, Functionalization of biomass carbonaceous aerogels: selective preparation of MnO_2@CA composites for supercapacitors, ACS Appl. Mater. Interfaces 6 (12) (2014) 9689–9697.
[37] Y. Zhao, W. Ran, J. He, Y. Huang, Z. Liu, W. Liu, Y. Tang, L. Zhang, D. Gao, F. Gao, High-performance asymmetric supercapacitors based on multilayer MnO_2/graphene oxide nanoflakes and hierarchical porous carbon with enhanced cycling stability, Small 11 (11) (2015) 1310–1319.
[38] H. Ma, J. He, D.-B. Xiong, J. Wu, Q. Li, V. Dravid, Y. Zhao, Nickel cobalt hydroxide @reduced graphene oxide hybrid nanolayers for high performance asymmetric supercapacitors with remarkable cycling stability, ACS Appl. Mater. Interfaces 8 (3) (2016) 1992–2000.
[39] C.H. Yu, C.H. Huang, C.S. Tan, A review of CO_2 capture by absorption and adsorption, Aerosol Air Qual. Res. 12 (5) (2012) 745–769.
[40] J. Rodriguez-Moreno, E. Navarrete-Astorga, E.A. Dalchiele, R. Schrebler, J.R. Ramos-Barrado, F. Martin, Vertically aligned ZnO@CuS@PEDOT core@shell nanorod arrays decorated with MnO_2 nanoparticles for a high-performance and semi-transparent supercapacitor electrode, Chem. Commun. 50 (42) (2014) 5652–5655.
[41] V. Augustyn, P. Simon, B. Dunn, Pseudocapacitive oxide materials for high-rate electrochemical energy storage, Energ. Environ. Sci. 7 (5) (2014) 1597–1614.
[42] M.J. Zhi, C.C. Xiang, J.T. Li, M. Li, N.Q. Wu, Nanostructured carbon-metal oxide composite electrodes for supercapacitors: a review, Nanoscale 5 (1) (2013) 72–88.
[43] W. Zhu, Z. Lu, G. Zhang, X. Lei, Z. Chang, J. Liu, X. Sun, Hierarchical $Ni_{0.25}Co_{0.75}(OH)_2$ nanoarrays for a high-performance supercapacitor electrode prepared by an in situ conversion process, J. Mater. Chem. A 1 (29) (2013) 8327–8331.
[44] C. Cui, J. Xu, L. Wang, D. Guo, M. Mao, J. Ma, T. Wang, Growth of $NiCo_2O_4$@$MnMoO_4$ nanocolumn arrays with superior pseudocapacitor properties, ACS Appl. Mater. Interfaces 8 (13) (2016) 8568–8575.
[45] F. Béguin, V. Presser, A. Balducci, E. Frackowiak, Carbons and electrolytes for advanced supercapacitors, Adv. Mater. 26 (14) (2014) 2219–2251.
[46] R. Mysyk, E. Raymundo-Piñero, F. Béguin, Saturation of subnanometer pores in an electric double-layer capacitor, Electrochem. Commun. 11 (3) (2009) 554–556.
[47] Z. Hu, L. Zu, Y. Jiang, H. Lian, Y. Liu, Z. Li, F. Chen, X. Wang, X. Cui, High specific capacitance of polyaniline/mesoporous manganese dioxide composite using KI-H_2SO_4 electrolyte, Polymers 7 (2015) 1939–1953.
[48] G. Gryglewicz, J. Machnikowski, E. Lorenc-Grabowska, G. Lota, E. Frackowiak, Effect of pore size distribution of coal-based activated carbons on double layer capacitance, Electrochim. Acta 50 (5) (2005) 1197–1206.
[49] X. Wang, J.Y. Liu, Y.Y. Wang, C.M. Zhao, W.T. Zheng, Ni(OH)(2) nanoflakes electrodeposited on Ni foam-supported vertically oriented graphene

nanosheets for application in asymmetric supercapacitors, Mater. Res. Bull. 52 (2014) 89–95.
[50] X.F. Lu, D.J. Wu, R.Z. Li, Q. Li, S.H. Ye, Y.X. Tong, G.R. Li, Hierarchical $NiCo_2O_4$ nanosheets@hollow microrod arrays for high-performance asymmetric supercapacitors, J. Mater. Chem. A 2 (13) (2014) 4706–4713.
[51] K.B. Hatzell, L. Fan, M. Beidaghi, M. Boota, E. Pomerantseva, E.C. Kumbur, Y. Gogotsi, Composite manganese oxide percolating networks as a suspension electrode for an asymmetric flow capacitor, ACS Appl. Mater. Interfaces 6 (11) (2014) 8886–8893.
[52] X. Wang, W.S. Liu, X.H. Lu, P.S. Lee, Dodecyl sulfate-induced fast faradic process in nickel cobalt oxide-reduced graphite oxide composite material and its application for asymmetric supercapacitor device, J. Mater. Chem. 22 (43) (2012) 23114–23119.
[53] X. Wang, A. Sumboja, M.F. Lin, J. Yan, P.S. Lee, Enhancing electrochemical reaction sites in nickel-cobalt layered double hydroxides on zinc tin oxide nanowires: a hybrid material for an asymmetric supercapacitor device, Nanoscale 4 (22) (2012) 7266–7272.